Numerical Approach to Modeling Fiber Motion During Melt Blowing

Y. C. Zeng,[1,2] Y. F. Sun,[1] X. H. Wang[1]

[1]*College of Textiles, Donghua University, Songjiang, Shanghai 201620, People's Republic of China*
[2]*Key Laboratory of Textile Science & Technology, Ministry of Education, Donghua University, Shanghai 201620, People's Republic of China*

Received 9 March 2010; accepted 2 June 2010
DOI 10.1002/app.32921
Published online 26 August 2010 in Wiley Online Library (wileyonlinelibrary.com).

ABSTRACT: Melt blowing involves applying a jet of hot air to an extruding polymer melt and drawing the polymer stream into microfibers. This study deals with the dynamic modeling of the instabilities and related processes during melt blowing. A bead-viscoelastic element model for fiber formation simulation in the melt blowing process was proposed. Mixed Euler-Lagrange approach was adopted to derive the governing equations for modeling the fiber motion as it is being formed below a melt-blowing die. The three-dimensional paths of the fiber whipping in the melt blowing process were calculated. Predicted parameters include fiber diameter, fiber temperature, fiber stress, fiber velocity, and the amplitude of fiber whipping. The mathematical model provides a clear understanding on the mechanism of the formation of microfibers during melt blowing.
 J Appl Polym Sci 119: 2112–2123, 2011

Key words: microfibers; melt blowing; modeling

INTRODUCTION

One of the most significant developments in recent years has been the technology to extrude extremely fine fibers while maintaining all the characteristics expected by textile manufacturers and consumers. Electrospinning, melt blowing, and melt spinning are the most commonly used processes to produce microfibers. Electrospinning can make fibers with the diameters in the range of 100 nm and even less; while the fibers produced via conventional melt spinning are usually not smaller than 10 μm. Melt blowing is a rapid, single-step process used to produce fibers with diameters exceeding 1–2 μm. It is finding applications in an increasing number of fields, such as filtration, absorbency, hygiene, and apparel. Multiorifice commercial melt blowing lines have the advantage of much lower cost than the multiorifice commercial electrospinning production lines. If melt blowing technology could be extended to nano-scale fiber sizes, it would penetrate new markets and enhance current product offerings. Therefore, a major focus of melt blowing research should be to extend the technology to nanofibers. To reach this goal, a fundamental understanding of the melt blowing process is important.

In melt blowing, fibers are produced by extruding a polymer melt through the spinneret and drawing down the extrudate with a jet of high-velocity hot air. Figure 1 shows the schematic of diagram of melt blowing. During melt blowing, the fiber undergoes bending instability, which is called whipping in electrospinning. This bending instability is attributed to the high velocity of the air. In this study, bending instability (or fiber vibration) in the melt blowing process is also called whipping, which was previously adopted by Ellison et al.[1] in their research on melt-blown nanofibers. The features of fast, chaotic and complicated make it difficult to study the melt blowing process theoretically as well as experimentally. Shambaugh and coworkers did a series work on understanding the melt blowing process. Uyttendaele and Shambaugh,[2] Rao and Shambaugh,[3] and Marla and Shambaugh,[4] respectively developed 1, 2, and 3D models to predict the fiber motion in melt blowing. The 2 and 3D models took into account the fiber vibrations. As to their experimental work, Shambaugh and coworkers[3,5–9] reported experimental measurements of fiber motion and fiber diameter using a single-orifice melt-blowing die. For example, Wu and Shambaugh[5] used laser Doppler velocimetry to measure the cone diameters of fiber vibrations. Rao and Shambaugh,[3] and Chhabra and Shambaugh[6] measured the fiber vibration with

Correspondence to: X. H. Wang (xhwang@dhu.edu.cn).
Contract grant sponsor: The National Natural Science Foundation of China; contract grant number: 10972052.
Contract grant sponsor: Foundation for the Author of National Excellent Doctoral Dissertation of the People's Republic of China; contract grant number: 2007B54.
Contract grant sponsor: Program for Century Excellent Talents in University; contract grant number: NCET-09-0285.

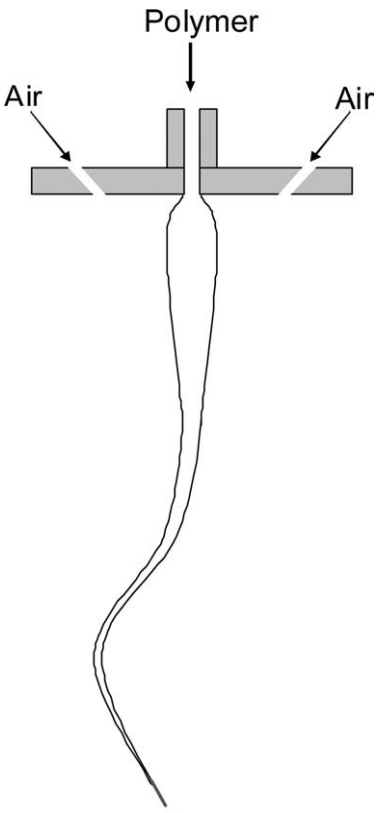

Figure 1 Schematic diagram of melt blowing process.

multiple-image flash photography. Recently, Beard et al.[10] used a high-speed camera (150,000 frame/s) to record the motion of a fiber below both a melt-blowing slot die and a melt-blowing swirl die. The photograph taken under the operation of a swirl die recorded a spiral motion of the fiber, which is the typical shape of the whipping motion in electrospinning.[11–13] Besides the researches of Shambaugh and coworkers, Chen and Huang[14] presented a 1D air drawing model of a polymer in the melt blowing process. Bresee and coworkers[15–17] reported experimental study of the melt blowing process in a commercial 600-orifice line.

Compared to the electrospinning research, much fewer has been done on the whipping dynamics in the melt blowing process. The physical mechanism of the electrospinning process is explained and described following several researchers.[11,12,18–22] And it is shown that the whipping motion (or bending instability), which is triggered by lateral perturbations, is the key physical element of the electrospinning process responsible for enormously strong stretching and formation of nanofibers. Shambaugh and coworkers did a series work on modeling and measuring fiber motion. The model developed by Shambaugh and coworkers accounts for the effect of whipping on attenuation. However, for the experimental conditions that they used, these effects (both measured and predicted effects) were small. Our work focuses on the whipping motion in the melt blowing process. Whipping in the electrospinning process is an electrically driven bending instability; while in the melt blowing process, it is an aerodynamic-driven bending instability, which has been described by Entov and Yarin.[23]

Modeling/simulation provides a rapid and low-cost way to understand the melt blowing process. In their theoretical work, Shambaugh and coworkers[2–4] divided the space below the melt-blowing die into a series of control volumes (CV). Each CV contains an element of the fiber. The fiber can be oriented in any direction within each CV. The external forces acting on a fiber element are the gravitational force, the aerodynamic force, and the rheological forces. And they made the assumption that the fiber did not offer any resistance to bending. As to the air velocity and temperature fields used in the simulation, experimentally measured data were adopted. The simulation results gave the information of fiber motion, including fiber vibration in melt blowing.

There are two approaches to describe the fluid motion, namely the Euler and the Lagrange approaches. The Euler approach describes the distributions of the variables in flow field at any time, while the Lagrange approach traces each particle from a certain time and describes its trajectory. The fiber motion path, i.e., the trajectory and deformation of the fiber in air flow field, is important to gain an insight into the formation of microfibers. In our previous work,[24] we adopted a mixed Euler-Lagrange approach to simulate the process of staple fibers into yarn with high-speed air technology. This approach described the air flow with the Euler approach, giving the distributions of the variable including velocity, pressure, and temperature. As to the fiber, the Lagrange approach was used, describing the trajectory of the fiber in the air flow. In this study, we develop a bead-viscoelastic element fiber model, and then adopt mixed Euler-Lagrange approach to simulate the three-dimensional fiber motion, especially the whipping motion in the process of melt blowing.

PHYSICAL MODEL AND GOVERNING EQUATIONS

Mathematical description of a fiber

Fiber is one class of slender particle, which differs from general particulates in two factors: (a) the aspect ratio of the fiber is large; (b) the fiber is flexible. In modeling, the flexible fiber is defined as: any segment of the fiber may stretch, bend, or rotate relative

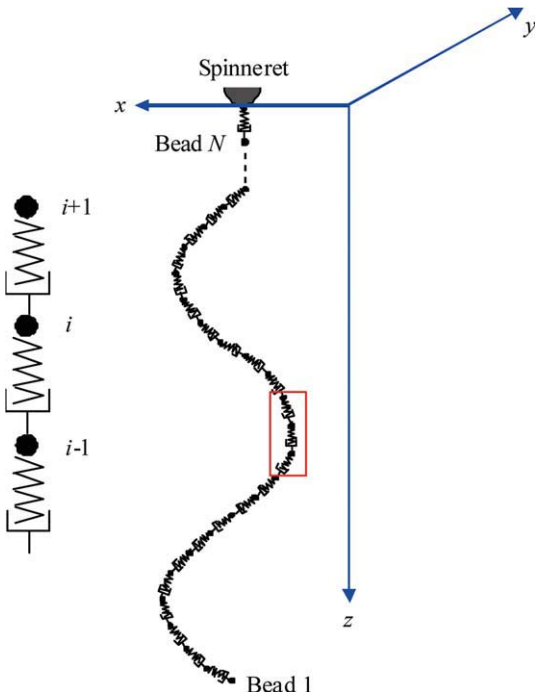

Figure 2 Schematic of a bead-viscoelastic element fiber model. [Color figure can be viewed in the online issue, which is available at wileyonlinelibrary.com.]

to the other segments. Figure 2 shows a fiber exiting from a spinneret of the melt-blowing die. We represent the melt-blown fiber by a model of a series of beads connected by viscoelastic elements. Each bead is considered to represent the center of mass of an element. A pair of adjacent beads, $i-1$ and i, form the fiber element $(i-1, i)$, and the length of the element $l_{i-1,i}$ is given by

$$l_{i-1,i} = \left[(x_i - x_{i-1})^2 + (y_i - y_{i-1})^2 + (z_i - z_{i-1})^2\right]^{1/2} \quad (1)$$

The total number of beads, N, increases over time as new beads are inserted at the top of Figure 2 to represent the flow of melt polymer into the fiber.

In our model, the mass of bead i, m_i, is contributed by its adjacent fiber elements $(i-1, i)$ and $(i, i+1)$, thus, m_i is described as

$$m_i = \frac{1}{2}\rho_f(A_{i-1,i}l_{i-1,i} + A_{i,i+1}l_{i,i+1}) \quad (2)$$

where ρ_f is the fiber (polymer) density, $A_{i-1,i}$ and $A_{i,i+1}$ are the fiber cross-sectional areas of fiber elements $(i-1, i)$ and $(i, i+1)$, respectively, and are described as

$$A_{i-1,i} = \frac{1}{4}\pi d_{i-1,i}^2 \quad (3a)$$

$$A_{i,i+1} = \frac{1}{4}\pi d_{i,i+1}^2 \quad (3b)$$

where $d_{i-1,i}$ and $d_{i,i+1}$ are the diameters of fiber elements $(i-1, i)$ and $(i, i+1)$, respectively. For the first bead, bead 1, m_1 is contributed by the element (1, 2).

Lagrange equations for fiber motion

The forces acting on bead i are the gravitational force, the air drag from the external air flow field, the viscoelastic force from the neighboring fiber elements, and the surface tension force tending to restore the rectilinear shape of the bending part of the fiber.

As is the case for the mass of bead i, the air drag for bead i is contributed by fiber elements $(i-1, i)$ and $(i, i+1)$. The air drag on bead i may be calculated by

$$\mathbf{F}_{di} = \frac{1}{2}(\mathbf{F}^i_{di-1,i} + \mathbf{F}^i_{di,i+1}) \quad (4)$$

where $\mathbf{F}_{di}$ is the air drag force on bead i, $\mathbf{F}^i_{di-1,i}$ is the drag on bead i contributed by fiber element $(i-1, i)$, and $\mathbf{F}^i_{di,i+1}$ is the drag on bead i contributed by $(i, i+1)$.

For the element $(i-1, i)$, the air drag can be written as

$$\mathbf{F}^i_{di-1,i} = \mathbf{F}^i_{fi-1,i} + \mathbf{F}^i_{Pi-1,i} \quad (5)$$

where $\mathbf{F}^i_{fi-1,i}$ is the skin friction drag on element $(i-1, i)$ for bead i, and $\mathbf{F}^i_{Pi-1,i}$ is the pressure drag on element $(i-1, i)$ for bead i.

To calculate the drag force on the fiber element, the local relative velocity between the air and the fiber is resolved into two components: axial and normal to the direction of the fiber element. Thus, the friction drag and the pressure drag can be expressed as

$$\mathbf{F}^i_{fi-1,i} = \frac{1}{2}C_f\rho_a v^2_{\mathrm{rt}i}\pi d_{i-1,i}l_{i-1,i} \quad (6)$$

and

$$\mathbf{F}^i_{Pi-1,i} = \frac{1}{2}C_P\rho_a v^2_{\mathrm{rn}i}d_{i-1,i}l_{i-1,i} \quad (7)$$

where ρ_a is the air density. $v_{\mathrm{rt}i}$ and $v_{\mathrm{rn}i}$ are relative velocities in axial and normal to the direction of the fiber element, respectively, at bead i.

In eqs. (6) and (7), C_f and C_P are the friction drag coefficient and the pressure drag coefficient. C_f is recommended to be a function of Reynolds number Re_l. Matsui[25] developed a form of a turbulent boundary layer a theoretical relation as

$$C_f = \beta(Re_{dt})^{-n} \quad (8)$$

in this relation for C_f there is no dependence on Re_l. Matsui attributed this independence to random

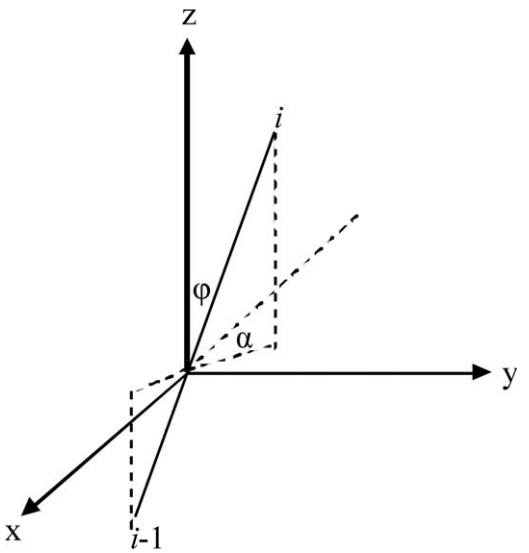

Figure 3 Orientation of a fiber element in the xyz coordinate system.

vibrations of the filament in melt spinning which cause there to be a constant average boundary layer thickness along the filament. Majumdar and Shambaugh[26] determined that $\beta = 0.78$ and $n = 0.61$ for melt blowing conditions. We adopt this relation and the values for our system. And Re_{dt} is defined as

$$Re_{dt} = \frac{\rho_a v_{\mathrm{rt}i} d_{i-1,i}}{\mu_a} \tag{9}$$

in which μ_a is the air dynamic viscosity. C_P is given from a plot of the pressure drag coefficient versus the Reynolds number $Re_{d\mathrm{n}}$ for a cylinder placed with its axis perpendicular to the direction of motion.[27] $Re_{d\mathrm{n}}$ is defined as

$$Re_{dn} = \frac{\rho_a v_{\mathrm{m}i} d_{i-1,i}}{\mu_a} \tag{10}$$

To calculate $v_{\mathrm{rt}i}$ and $v_{\mathrm{rn}i}$, we adopt Marla and Shambaugh's method,[4] and the following eqs. (11)–(14) are derived from equations in the literature.[4] Considering a fiber element ($i-1$, i) as shown in Figure 3, a unit vector $\mathbf{f}_t$ that is parallel to the fiber axis is

$$\mathbf{f}_t = \sin(\varphi)\cos(\alpha) + \mathbf{i} + \sin(\varphi)\sin(\alpha) + \mathbf{j} + \cos(\varphi)\mathbf{k} \tag{11}$$

where the angle φ is the angle between the fiber axis and the z axis. The projection of the fiber element upon the x-y plane makes an angle α with the x axis. $\mathbf{i}$, $\mathbf{j}$, and $\mathbf{k}$ are unit vectors in the xyz coordinate system.

To determine $\mathbf{f}_n$, the unit vector normal to the fiber element, we need first to define the plane in which $\mathbf{f}_n$ lies. The relative velocity at bead i is

$$\mathbf{v}_{ri} = (v_{aix} - v_{fix})\mathbf{i} + (v_{aiy} - v_{fiy}) + \mathbf{j}(v_{aiz} - v_{fiz})\mathbf{k} \tag{12}$$

where $\mathbf{v}_{ai}$ and $\mathbf{v}_{fi}$ are air and fiber velocities at bead i, respectively. Let us define

$$\mathbf{u} = \mathbf{v}_{ri} \times \mathbf{f}_t \tag{13}$$

Then

$$\mathbf{f}_n = \frac{\mathbf{f}_t \times \mathbf{u}}{||\mathbf{f}_t \times \mathbf{u}||} \tag{14}$$

The axial and normal components of the relative velocity with respect to the fiber element direction are then

$$v_{rti} = (\mathbf{v}_{ri} \cdot \mathbf{f}_t) \cdot \mathbf{f}_t \tag{15}$$

$$v_{mi} = (\mathbf{v}_{ri} \cdot \mathbf{f}_n) \cdot \mathbf{f}_n \tag{16}$$

Therefore, the friction drag $\mathbf{F}^i_{fi-1,i}$ and the pressure drag $\mathbf{F}^i_{Pi-1,i}$ can be calculated from eqs. (6) and (7). And the total drag for the element ($i-1$, i), $\mathbf{F}^i_{di-1,i}$ is calculated from eq. (5).

The melt-blown fiber is modeled as a series of beads connected by viscoelastic elements. We use Maxwell model to describe rheological behavior of the polymer. The tensile stress acting along the fiber element ($i-1$, i), $\sigma_{i-1,i}$, is given by

$$\frac{d\sigma_{i-1,i}}{dt} = G\frac{1}{l_{i-1,i}}\frac{dl_{i-1,i}}{dt} - \frac{G}{\mu}\sigma_{i-1,i} \tag{17}$$

where t is time, G and μ are the elastic modulus and viscosity of the polymer, respectively.

The net viscoelastic force acting on bead i, $\mathbf{F}_{vei}$, is

$$\mathbf{F}_{vei} = \frac{\pi d^2_{i,i+1}}{4}\sigma_{i,i+1}\left[\frac{x_{i+1}-x_i}{l_{i,i+1}}\mathbf{i} + \frac{y_{i+1}-y_i}{l_{i,i+1}}\mathbf{j} + \frac{z_{i+1}-z_i}{l_{i,i+1}}\mathbf{k}\right] - \frac{\pi d^2_{i-1,i}}{4}\sigma_{i-1,i}\left[\frac{x_i-x_{i-1}}{l_{i-1,i}}\mathbf{i} + \frac{y_i-y_{i-1}}{l_{i-1,i}}\mathbf{j} + \frac{z_i-z_{i-1}}{l_{i-1,i}}\mathbf{k}\right] \tag{18}$$

where $\mathbf{r}_i = \mathbf{i}x_i + \mathbf{j}y_i + \mathbf{k}z_i$ is the position of bead i in the xyz coordinate system.

Consider a fiber part ($i-1$, i, $i+1$), the equilibrium shape of the fiber part is rectilinear. When the fiber part is bent, there is a surface tension force acting on bead i, and tending to restore the rectilinear shape of the bending part of the fiber. The surface tension force on bead i is calculated by the fiber elements ($i-1$, i) and (i, $i+1$), and given by

$$\mathbf{F}_{bi} = \frac{\eta\pi\left(\frac{d_{i-1,i}+d_{i,i+1}}{2}\right)^2 k_i}{4(x_i^2 + y_i^2)^{1/2}}[\mathbf{i}x_i + \mathbf{j}y_i] \tag{19}$$

where η is the surface tension coefficient, k_i is the fiber part curvature. k_i is written as

$$k_i = |\mathbf{r}_i' \times \mathbf{r}_i''| \tag{20}$$

In the computer model, $\mathbf{r}_i'$ and $\mathbf{r}_i''$ can be written as

$$\mathbf{r}_i' = \frac{\mathbf{r}_{i+1} - \mathbf{r}_{i-1}}{l_{i-1,i} + l_{i,i+1}} \tag{21}$$

and

$$\mathbf{r}_i'' = \frac{\mathbf{r}_{i+1} - 2\mathbf{r}_i + \mathbf{r}_{i-1}}{l_{i-1,i} l_{i,i+1}} \tag{22}$$

As vectors $\mathbf{r}_i'$ and $\mathbf{r}_i''$ are perpendicular to each other, k_i can be written as

$$k_i = |\mathbf{r}_i'| \cdot |\mathbf{r}_i''| \tag{23}$$

Therefore, we obtain the equation governing the motion of bead i in the following form

$$m_i \frac{d^2\mathbf{r}_i}{dt^2} \mathbf{F}_{di} + \mathbf{F}_{vei} + \mathbf{F}_{bi} + m_i g \tag{24}$$

where $\mathbf{F}_{di}$, $\mathbf{F}_{vei}$, and $\mathbf{F}_{bi}$ are described in eqs. (4), (18), and (19). $m_i g$ is the gravity of bead i.

In our model, the heat transfer within the fiber is neglected. The energy equation is described as:

$$m_i C_i \frac{dT_i}{dt} = -h\pi \frac{d_{i-1,i} + d_{i,i+1}}{2} \frac{l_{i-1,i} + l_{i,i+1}}{2} (T_i - T_{ai}) \tag{25}$$

where C_i is the polymer heat capacity, T_i is the temperature of fiber bead i, T_{ai} is the air temperature at bead i, and h is the convective heat transfer coefficient.

Perturbation of the rectilinear fiber segment

Perturbations of the lateral position and lateral velocity of the fiber lead to the development of the bending instability, and become the observed whipping motion. To model the 3D whipping motion, an initial perturbation should be added. In our model, the initial perturbation is added by inserting small displacements in x and y coordinates of bead i

$$x_i = a \sin(\omega t) \tag{26a}$$

$$y_i = a \cos(\omega t) \tag{26b}$$

here a is the initial perturbation amplitude, and ω is the initial perturbation frequency.

Euler equations for air flow

In this research, the airflow field is obtained by solving the Navier-Stokes equations in Euler scheme through the commercial software FLUENT 6.2.

$$\frac{\partial \rho_a}{\partial t} + \mathrm{div}(\rho_a \mathbf{V}_a) = 0 \tag{27a}$$

$$\rho_a \frac{D\mathbf{V}_a}{Dt} = \rho_a \mathbf{F}_a + \mathrm{div}(\tau) \tag{27b}$$

$$\frac{\partial(\rho_a T_a)}{\partial t} + \mathrm{div}(\rho_a \mathbf{V}_a T_a) = \mathrm{div}\left(\frac{h}{C_a} \mathrm{grad} T_a\right) + S_T \tag{27c}$$

Equations (27a)–(27c) express the mass conservation, momentum conservation and energy conservation of the airflow, where τ is the stress caused by viscosity of air, $\mathbf{F}_a$ is the body force, C_a is the air heat capacity, and S_T is the vicious dissipation term.

SOLUTION PROCEDURE

According to the mathematical model described earlier, the time evolution of the fiber motion is determined by the following procedure:

1. The air velocity and temperature fields are calculated, using Fluent 6.2 software.
2. At $t = 0$, the fiber includes two beads, bead 1 and bead 2. The distance between bead 2 and the spinneret exit, as well as the distance between bead 1 and bead 2, $l_{1,2}$, are set to be a small distance, say $L_0 = 0.5$ mm. The stresses $\sigma_{i-1,i}$ and $\sigma_{i,i+1}$ are set to be zero. The initial velocity of bead i, $d\mathbf{r}_i/dt$, is determined by the polymer flow rate Q. The initial temperature T_i is set to be the temperature in commercial production, say 310°C. Air velocity and temperature at the position of bead i, are read.
3. For a given time t, eqs. (24) and (25) are solved after solving their correlate eqs. (4), (18), and (19). All the variables related to bead i, including the stresses $\sigma_{i-1,i}$ and $\sigma_{i,i+1}$, the position $\mathbf{r}_i$, the temperature T_i, the length of the fiber elements $l_{i-1,i}$, and the diameter of the fiber element $d_{i-1,i}$, are obtained simultaneously. The velocity of bead i, $\mathbf{v}_{fi}$, is obtained for the next step.
4. With the obtained values of the above variables, the new values of all the variables at time $t+\Delta t$ are calculated numerically.
5. The last bead pulled out of the spinneret is bead $i = N$. When the distance between this bead and the spinneret becomes long enough, say $2L_0$, a new bead $i = N+1$ is inserted at the initial distance, L_0, from the spinneret exit. At the same time, the perturbation eqs. (26a) and (26b) are added.

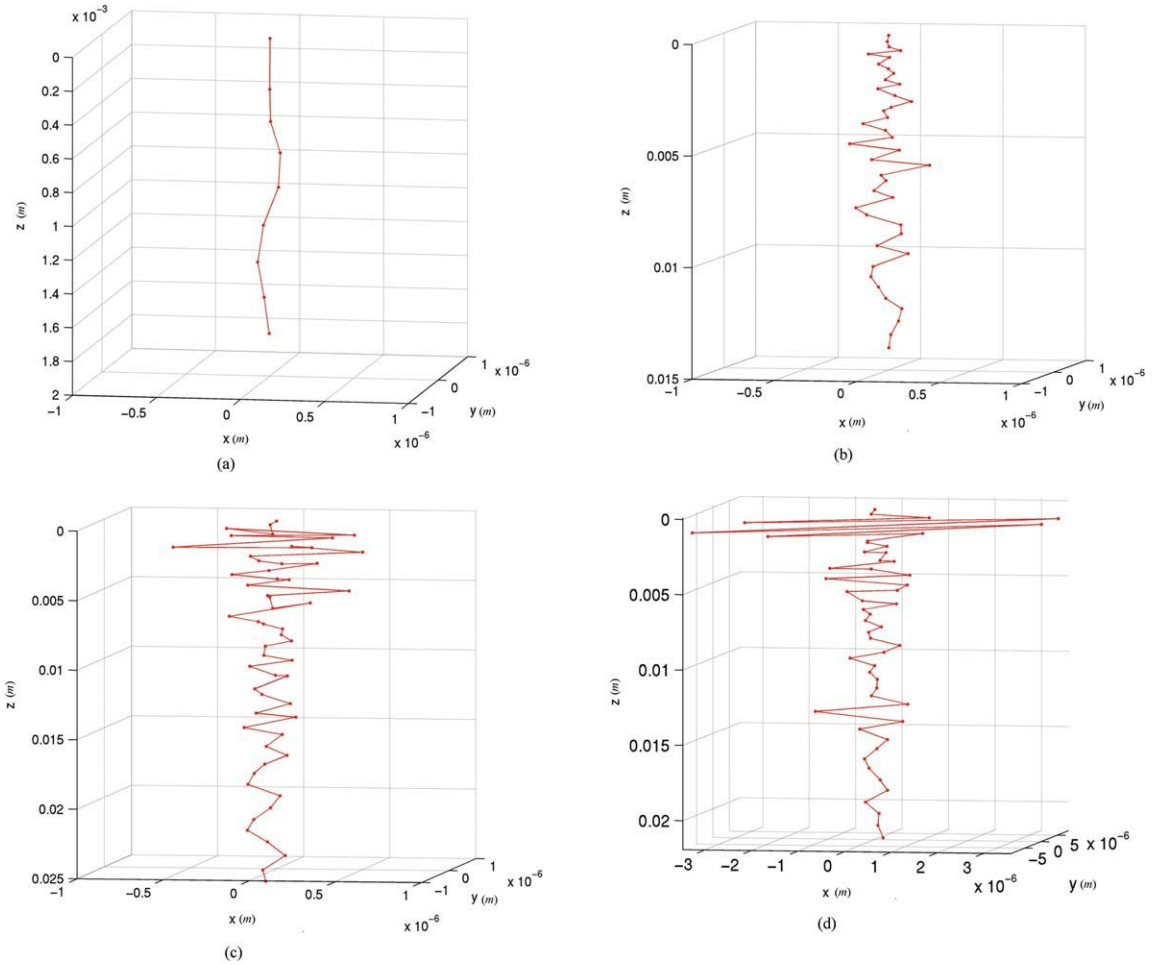

Figure 4 The time evolution of a whipping development for the simulation at low air velocity annular die. (a) $t = 0.255$ s, (b) 0.265 s, (c) 0.275 s, and (d) 0.295 s. [Color figure can be viewed in the online issue, which is available at wileyonlinelibrary.com.]

6. With iterations including the above procedure from the second to the third steps, we can follow the positions of all beads and obtain the path of the fiber motion in evolutionary time.

In our model, the Lagrange approach determines the stop-point as the point at which the air velocity and the fiber velocity become equal.

RESULTS AND DISCUSSION

In the modeling work of Shambaugh and coworkers,[2–4] they used experimentally measured air velocity and temperature of a single-orifice melt-blowing annular die as inputs to the model. In our study, two cases were conducted. To verify the model developed in this work, we first applied our model to the annular die with 110 m/s air velocity that Shambaugh and coworkers studied. The simulation results were compared with Shambaugh and coworkers' predictions and experimental results. Then, the approach developed in this work was applied to a melt-blowing slot die with the air velocity used in commercial production. These two cases are referred to as the "low air velocity annular die" and "high air velocity slot die."

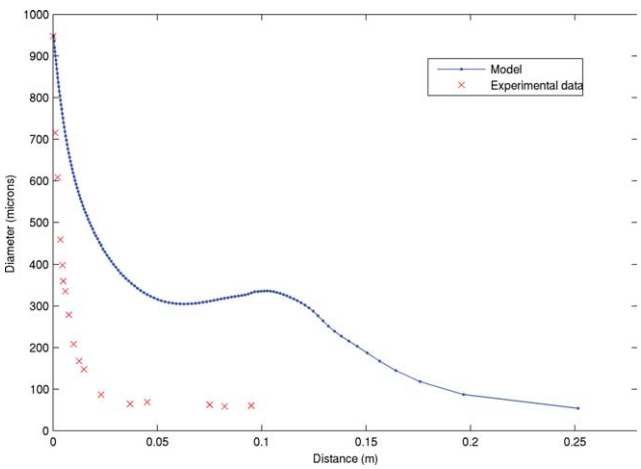

Figure 5 The fiber diameter profile for the simulation at low air velocity annular die. [Color figure can be viewed in the online issue, which is available at wileyonlinelibrary.com.]

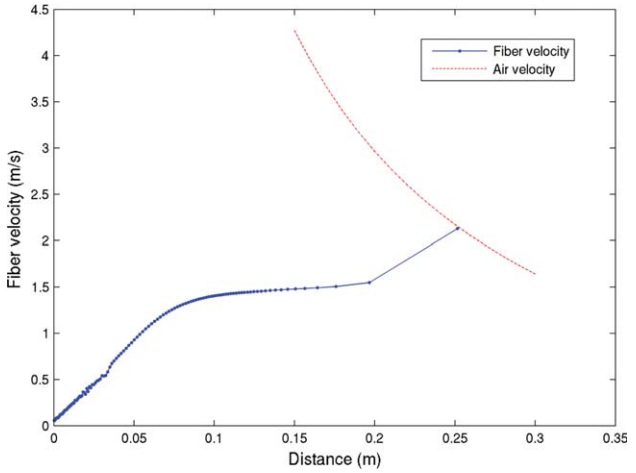

Figure 6 The fiber velocity profile for the simulation at low air velocity annular die. [Color figure can be viewed in the online issue, which is available at wileyonlinelibrary.com.]

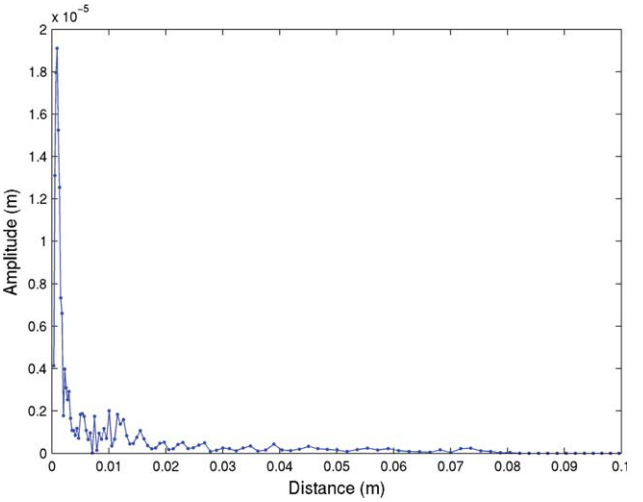

Figure 8 The whipping amplitude profile for the simulation at low air velocity annular die. [Color figure can be viewed in the online issue, which is available at wileyonlinelibrary.com.]

Low air velocity annular die

We begin with the calculation of the trajectory of the fiber motion. Figure 4(a–d) illustrate the development of a typical fiber path. The small perturbation, eqs. (26), develops into a whipping motion. The parameters used in the calculation include polymer properties, air properties, and processing parameters. The polymer property parameters are as follows: elastic modulus $G = 2.8 \times 10^4$ Pa, surface tension coefficient $\eta = 0.7$ kg/s^2, initial viscosity $\mu = 38.3787$ Pa·s, initial density $\rho_f = 598.28$ kg/m^3, and initial heat capacity $C_i = 1777.8$ J/kg·K; The air parameters used are: air density $\rho_a = 1.293$ kg/m^3, air dynamic viscosity $\mu_a = 0.297 \times 10^{-4}$ Pa·s, and convective heat transfer coefficient $h = 0.026$ W/m^2·K; The initial processing parameters are set as follows: initial fiber diameter is 0.949×10^{-3} m (949 μm), initial length $L_0 = 0.2 \times 10^{-3}$ m, initial air temperature is 385°C, initial polymer temperature is 310°C, initial fiber velocity is 0.06 m/s, polymer flow rate $Q = 1.6$ g/min, initial perturbation amplitude $a = 10^{-3}L_0$, and initial perturbation frequency $\omega = 10^4$ s^{-1}.

Figure 5 shows the predicted fiber diameter as a function of distance from the spinneret for our simulation. Also shown are the Uyttendaele's[2] experimental data for comparison. For an initial diameter of 949 μm, we predict the final fiber diameter is 54.135 μm at $t = 0.3036$ s. Marla and Shambaugh[4] predicted a final fiber diameter of 40.5 μm. As can be seen, the simulation results show the trends which remain in agreement with experimental data and Marla and Shambaugh's simulation results, though the predicted fiber attenuation is not so rapid when it is close to the spinneret. The plateau

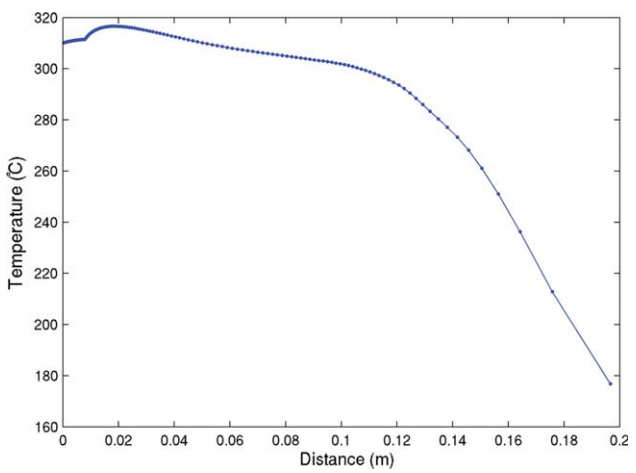

Figure 7 The fiber temperature profile for the simulation at low air velocity annular die. [Color figure can be viewed in the online issue, which is available at wileyonlinelibrary.com.]

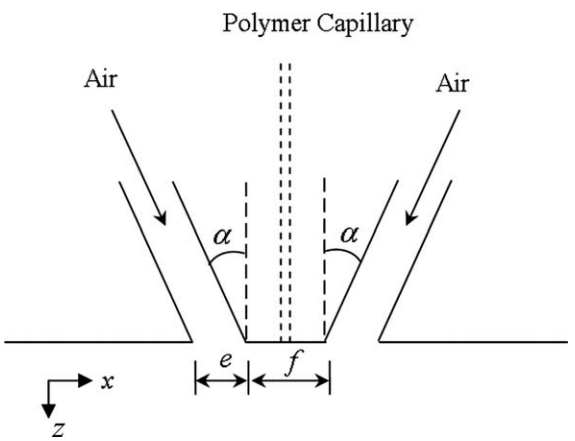

Figure 9 Basic profile of a melt-blowing slot die.

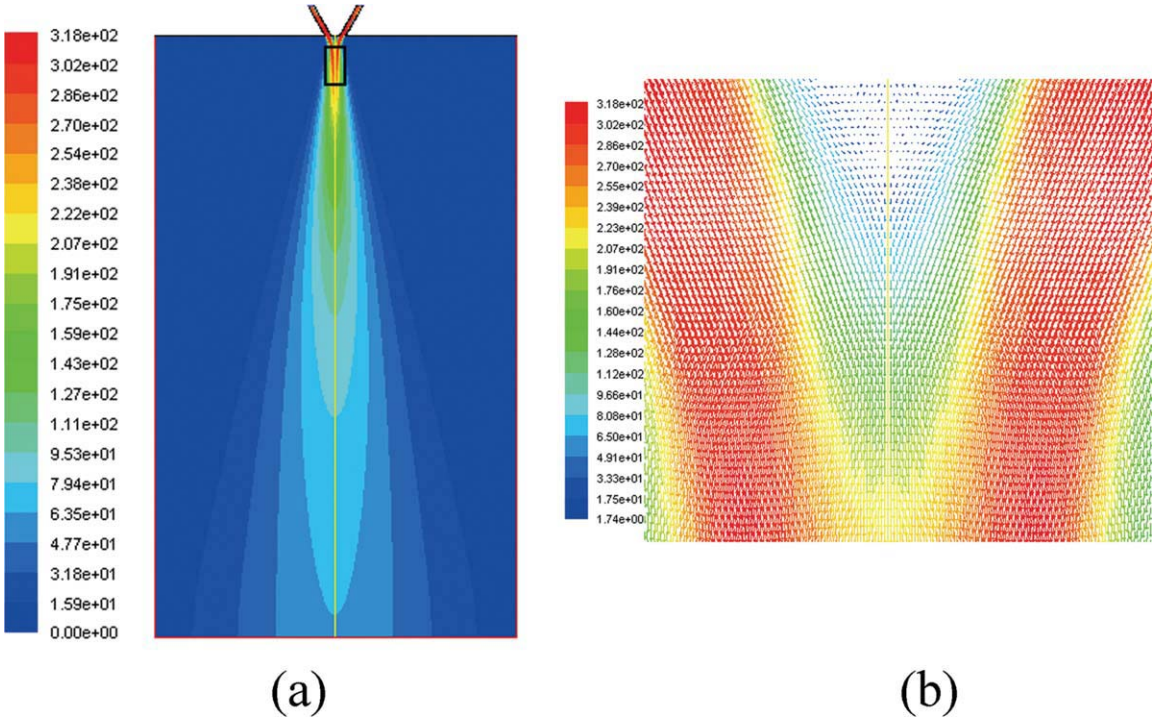

Figure 10 Contour of the air velocity field. (a) total velocity magnitude, (b) velocity vector field close to die. [Color figure can be viewed in the online issue, which is available at wileyonlinelibrary.com.]

around $z = 10$ cm in the fiber diameter profile corresponds to the plateau in the fiber velocity profile shown in Figure 6. In this area, the velocity differences between adjacent beads are small, leading to a small stretch of the fiber, and subsequently the small changes in fiber diameter. It is obvious that the fiber is accelerated by the high-speed air jet so that the fiber velocity increases steadily. When the distance far from the spinneret is around 25 cm, the fiber velocity and the air velocity are equal, which indicates the end of the simulation of the melt blowing process.

Figure 7 provides the fiber temperature profile. The values and shape of fiber temperature profile are almost the same as Marla and Shambaugh's[4] simulation results. Since the air temperature is higher than the polymer temperature, the fiber temperature increased as it ejected from the spinneret and contact the hot air. Then the temperature decays until it reaches the solidification point.

Figure 8 illustrates the whipping amplitude profile. The whipping amplitude is defined as the maximum lateral displacement at position z and is calculated as $(x_{max}^2 + y_{max}^2)^{1/2}$. Unlike Shambaugh and coworkers' amplitude prediction, we simulate a rapid increase of the amplitude close to the die. Then the whipping amplitude decays rapidly. It should be mentioned that the way for us to add the initial perturbation is different from that of Shambaugh and coworkers. Marla and Shambaugh[4] inserted an initial slope of $\Delta x/\Delta z = 10^{-5}$ in the x direction and a slope of $\Delta y/\Delta z = 10^{-5}$ in the y direction; While we consider the helical disturbance of the fiber axis.

In general, our simulation results show fair accordance with the Shambaugh and coworkers'

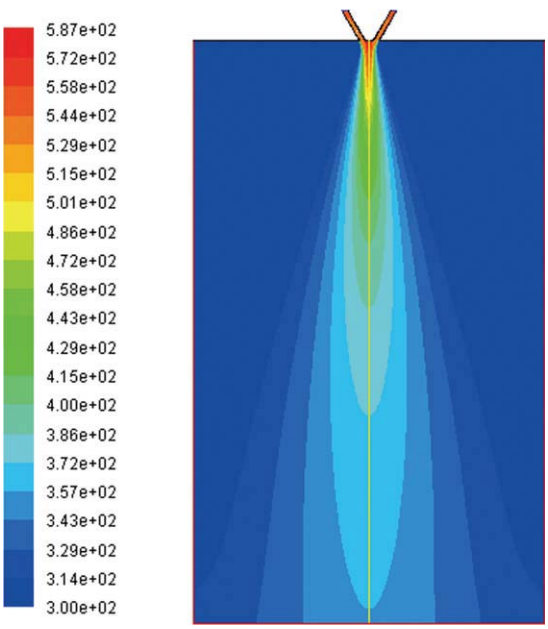

Figure 11 Contour of the air temperature field. [Color figure can be viewed in the online issue, which is available at wileyonlinelibrary.com.]

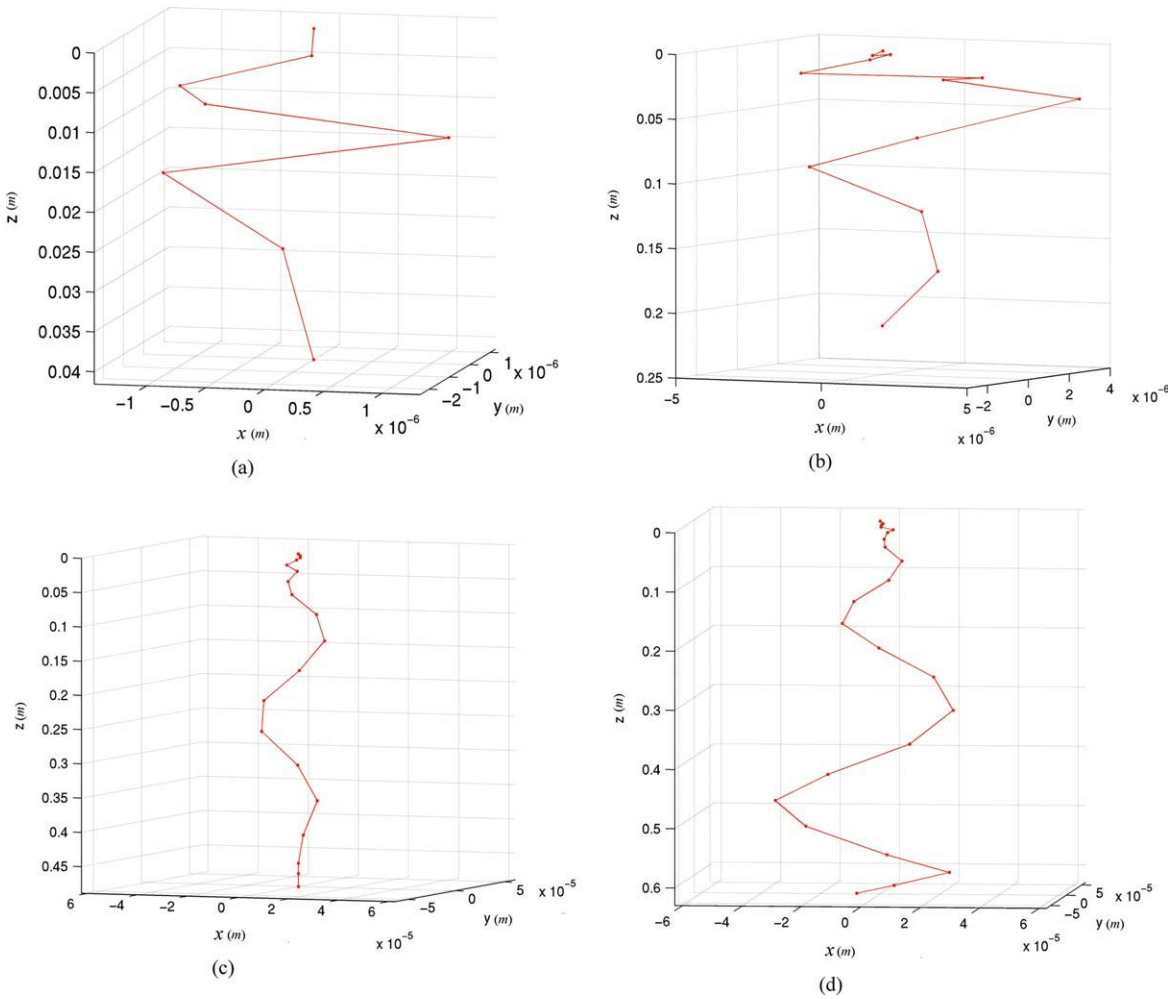

Figure 12 The time evolution of a whipping development for the simulation at high air velocity slot die. (a) $t = 0.04$ s, (b) 0.05 s, (c) 0.06 s, and (d) 0.07 s. [Color figure can be viewed in the online issue, which is available at wileyonlinelibrary.com.]

experimental and modeling work. The air velocities used in Shambaugh's work are much smaller than those in commercial melt blowing production, which are usually subsonic and supersonic. Nowadays, the slot die is predominant in the production of melt-blown fibers because of the "infinite" length of the slot. In the next case, the proposed mixed Euler-Lagrange approach is applied to simulate a fiber motion in a melt-blowing slot die with the air velocity used in commercial production.

High air velocity slot die

The basic profile of a melt-blowing slot die is shown in Figure 9. The parameters for the die structure in this simulation are: slot width $e = 1.0$ mm, nose piece width $f = 1.5$ mm, and slot angle $\alpha = 30°$. The Euler approach gives the simulation results of the airflow field. Figures 10 and 11 respectively display the contours of the air velocity field and air temperature field below the slot die. Figure 10(a) shows the velocity field over large distance from the air slots of the die. Figure 10(b) shows the velocity vectors, with velocity arrows, at the position of the window in Figure 10(a). The air velocity ejecting from the spinneret is 280 m/s.

The time evolution of the fiber path is shown in Figure 12(a–d). The initial parameters used in this calculation are different from those used in last case. Here, the initial length $L_0 = 2 \times 10^{-3}$ m and initial fiber velocity is 0.5 m/s. The path also displays a whipping motion generally similar to that shown in Figure 4. The fewer beads displayed in the fiber path than in Figure 4 is attributed to the larger initial length and the larger stretch in high-velocity air field.

Figure 13 shows the predicted fiber diameter as a function of distance from the spinneret. For an initial diameter of 400 μm, which is usually used in commercial production, we predict the final fiber diameter is 78.63 μm at $t = 0.07226$ s. As can be seen, the draw ration is smaller than that in Figure 5, for we

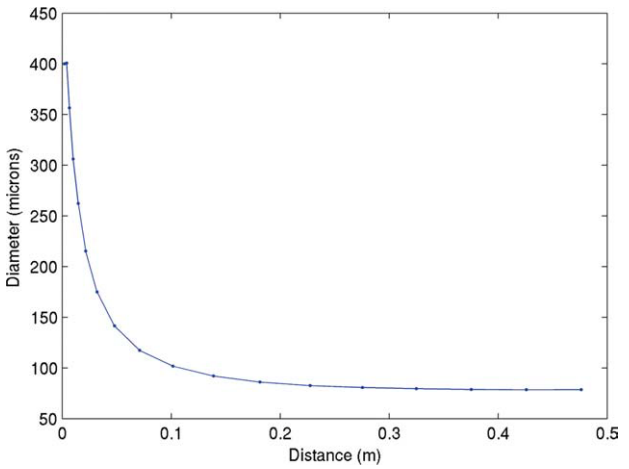

Figure 13 The fiber diameter profile for the simulation at high air velocity slot die. [Color figure can be viewed in the online issue, which is available at wileyonlinelibrary.com.]

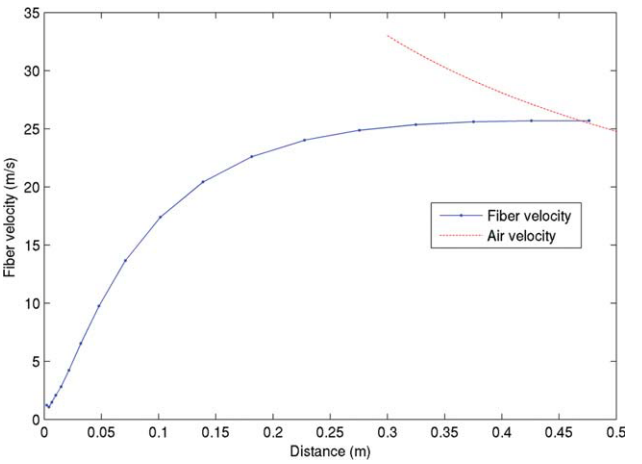

Figure 15 The fiber velocity profile for the simulation at high air velocity slot die. [Color figure can be viewed in the online issue, which is available at wileyonlinelibrary.com.]

used a bigger flow rate of polymer. The melt-blown fiber diameters in commercial production are always under 5 μm. Studies of multiorifice melt blowing operation at commercial speed by Bresee and coworkers[15–17] have shown that fiber diameter was reduced to about 15% its original size (from 368 μm to about 60 μm) after traveling less than 1 cm from the die. Our simulation shows that fiber diameter attenuation near the die is not as fast as their observation. The under-prediction of the draw ratio seems to be a shortage of our model. In our model, the draw ratio is mainly determined by the inflow velocity of the polymer melt and its final velocity. The effects of polymer properties are not taken into account, which will be improved in the future. On the other hand, the larger predicted fiber diameter may be explained by the different dies used in simulation and in commercial production. We adopted a single-hole melt blowing die in the simulation; while commercial melt blowing lines employ a mutiorifice design composed of a linear bank of holes more than a meter in length with hole diameters approximately 200–600 μm spaced at 10–20 holes/cm. Bresee and coworkers[15–17] observed that fiber contact and entanglement in a commercial multiorifice die also play roles in fiber attenuation.

The profiles of fiber stress, fiber velocity, and fiber temperature are illustrated in Figures 14–16, respectively. The predicted contours of fiber stress and fiber temperature show considerable accordance with the published experimental data of Bansal and Shambaugh.[9] Bresee and coworkers[15–17] provided on-line measurements of fiber velocity. They revealed that mean fiber velocity was very slow at

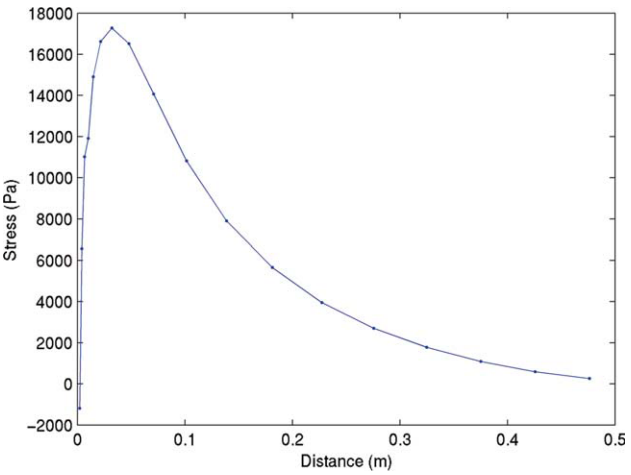

Figure 14 The fiber stress profile for the simulation at high air velocity slot die. [Color figure can be viewed in the online issue, which is available at wileyonlinelibrary.com.]

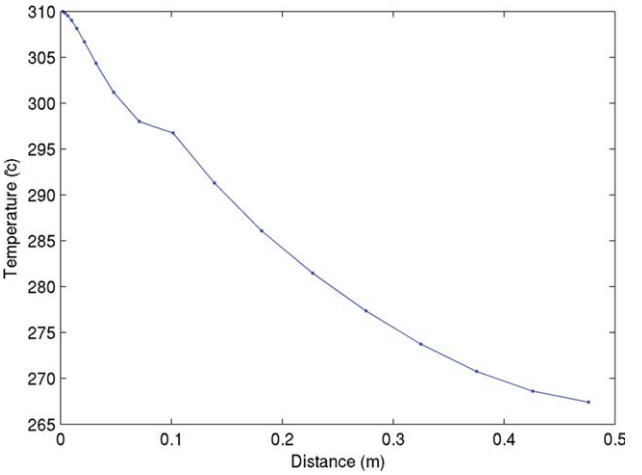

Figure 16 The fiber temperature profile for the simulation at high air velocity slot die. [Color figure can be viewed in the online issue, which is available at wileyonlinelibrary.com.]

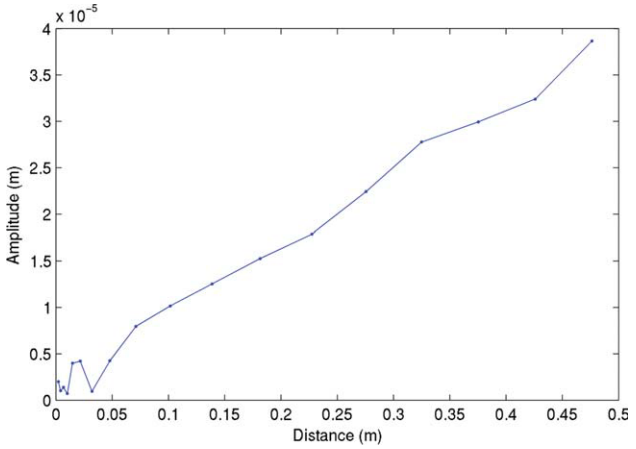

Figure 17 The whipping amplitude profile for the simulation at high air velocity slot die. [Color figure can be viewed in the online issue, which is available at wileyonlinelibrary.com.]

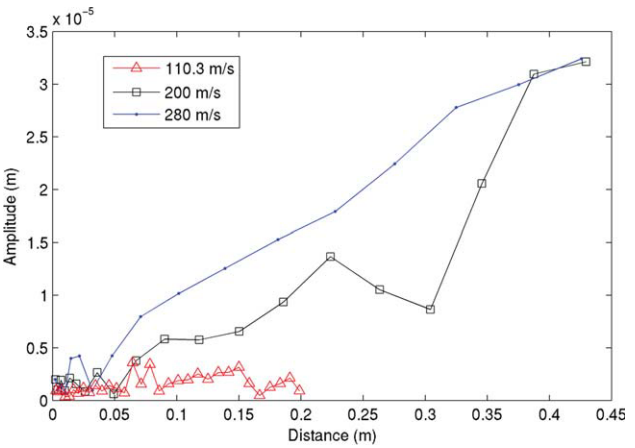

Figure 19 Effect of the initial air velocity on the predicted whipping amplitude profile. [Color figure can be viewed in the online issue, which is available at wileyonlinelibrary.com.]

the die but fibers quickly accelerated and reached the maximum velocity of around 60 m/s at about 5 cm from the die. Our simulation results (Fig. 15) show that fiber acceleration lasts for a longer distance (15 cm from the spinneret). And we predict a maximum velocity of 25 m/s.

Figure 17 illustrates the amplitude profile of the fiber whipping. Unlike the profile predicted in "low air velocity annular die," in this case, we predict a gradually growing whipping as time develops. Beard et al.[10] measured fiber vibration during melt blowing, and revealed that the amplitude of vibration increases from around 1 to 2.5 mm. Like the experiment, our simulation results show that amplitude increases with increasing distance from the die. However, we predict much smaller amplitude all over the air drawing axis. It should be mentioned that this article is the first step for our study on whipping motion in the melt blowing process. Further theoretical and experimental studies will focus on this subject. In our recent work,[28] the effect of perturbation on whipping motion in electrospinning was studied using experimental and modeling methods. In our future work, we will follow with interest of the perturbation effect on the whipping motion in the melt blowing process.

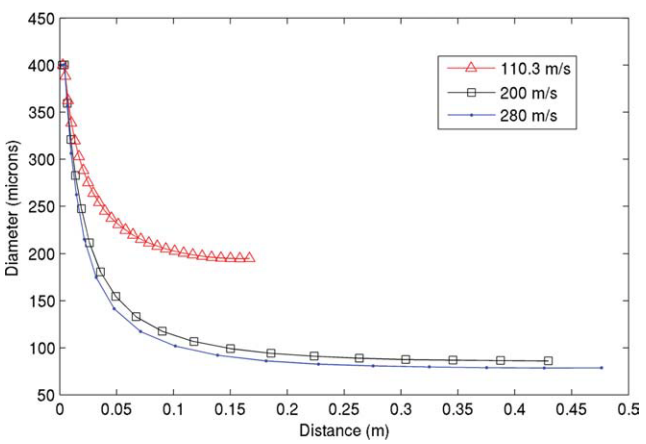

Figure 18 Effect of the initial air velocity on the predicted fiber diameter profile. [Color figure can be viewed in the online issue, which is available at wileyonlinelibrary.com.]

Figures 18 and 19 show how air velocity affects the predicted fiber diameter and whipping amplitude. Flow fields are considered that have initial air velocities of 110, 200, and 280 m/s. As expected, the higher velocities cause much more attenuation of the fibers, and the final diameters are smaller when the air velocity is high. The experimental work of Beard et al.[10] shows that (a) the amplitude increases as the distance from the die increases and (b) the amplitude is higher at an higher air velocity (air flow rate). Our model predicts the same trends that are exhibited by the experimental data.

CONCLUSIONS

We have proposed a method for modeling the fiber motion in the melt blowing process. The fiber model describes the character of large aspect ratio, viscoelasticity and flexibility of the fiber. Therefore, it can be used to simulate the fiber formation in melt blowing process. Mathematical model is developed using mixed Euler-Lagrange approach, which treats the air flow by the Euler approach and predicts the fiber motion by the Lagrange approach.

The proposed approach is applied to simulate the fiber motion in melt blowing process. The three-dimensional paths of fiber motion are calculated. The fiber path shows a small perturbation developing into the whipping. The results of predicted fiber

diameter, fiber temperature, fiber stress, fiber velocity, and fiber whipping amplitude are compared with the experimental data in the literature, as well as Shanbaugh and coworkers' simulation results. The results for slow and fast air speed show the trends which remain in agreement with experimental observations. Nevertheless, the model underpredicts the fiber attenuation and whipping amplitude. The mathematical model provides an insight into the mechanism of the formation of microfibers during melt blowing.

References

1. Ellison, C. J.; Phatak, A.; Giles, D. W.; Macosko, C. W.; Bates, F. S. Polymer 2007, 48, 3306
2. Uyttendaele, M. A. J.; Shambaugh, R. L. AIChE J 1990, 36, 175.
3. Rao, R. S.; Shambaugh, R. L. Ind Eng Chem Res 1993, 32, 3100.
4. Marla, V. T.; Shambaugh, R. L. Ind Eng Chem Res 2003, 42, 6993.
5. Wu, T. T.; Shambaugh, R. L. Ind Eng Chem Res 1992, 31, 379.
6. Chhabra, R.; Shambaugh, R. L. Ind Eng Chem Res 1996, 35, 4366.
7. Bansal, V.; Shambaugh, R. L. Ind Eng Chem Res 1998, 37, 1799.
8. Bansal, V.; Shambaugh, R. L. Tappi J 1998, 81, 199.
9. Bansal, V.; Shambaugh, R. L. Ind Eng Chem Res 1998, 37, 1799.
10. Beard, J. H.; Shambaugh, R. L.; Shambaugh, B. R.; Schmidtke, D. W. Ind Eng Chem Res 2007, 46, 7340.
11. Shin, Y. M.; Hohman, M. M.; Brenner, M. P.; Rutlege, G. C. Polymer 2001, 42, 9955.
12. Reneker, D. H.; Yarin, A. L.; Fong, H.; Koombhongse, S. J Appl Phys 2000, 87, 4531.
13. Theron, S. A.; Yarin, A. L.; Zussman, E.; Kroll, E. Polymer 2005, 46, 2889.
14. Chen, T.; Huang, X. B. Textile Res J 2003, 73, 651.
15. Yin, H.; Yan, Z. Y.; Bresee, R. R. Int Nonwovens J 1999, 8, 60.
16. Yin, H.; Yan, Z. Y.; Co, W. C.; Bresee, R. R. Int Nonwovens J 2000, 9, 25.
17. Bresee, R. R.; Ko, W. C. Int Nonwoven J 2003, 12, 21.
18. Shin, Y. M.; Hohman, M. M.; Brenner, M. P.; Rutlege, G. C. Appl Phys Lett 2001, 78, 1149.
19. Hohman, M. M.; Shin, Y. M.; Rutledge, G. C.; Brenner, M. P. Phys Fluids 2001, 13, 2201.
20. Hohman, M. M.; Shin, Y. M.; Rutledge, G. C.; Brenner, M. P. Phys Fluids 2001, 13, 2221.
21. Yarin, A. L.; Koombhongese, S.; Reneker, D. H. J Appl Phys 2001, 89, 3018.
22. Yarin, A. L.; Koombhongse, S.; Reneker, D. H. J Appl Phys 2002, 90, 4836.
23. Entov, V. M.; Yarin, A. L. J Fluid Mech 1984, 140, 91.
24. Zeng, Y. C.; Yang, J. P.; Yu, C. W. Appl Math Model 2005, 29, 253.
25. Matsui, M. Trans Soc Rheol 1976, 20, 465.
26. Majumdar, B.; Shambaugh, R. L. J Rheol 1990, 34, 591.
27. Mott, R. L. Applied Fluid Mechanics; Bell & Howell Company: Ohio, 1979, 351.
28. Yang, J. P.; Zeng, Y. C.; Pei, Z. G.; Wang, X. H. J Appl Polym Sci 2010, 115, 2508.